# Density functional simulations of pressurized Mg-Zn and Al-Zn alloys

Mohammad Alidoust [●],[1] David Kleiven,[1] and Jaakko Akola [●][1,2]

[1]*Department of Physics, Norwegian University of Science and Technology (NTNU), NO-7491 Trondheim, Norway*
[2]*Computational Physics Laboratory, Tampere University, FI-30014 Tampere, Finland*

Binary Mg-Zn and Al-Zn alloys have been investigated theoretically under static isotropic pressure. The stable phases of these binaries on both initially hexagonal-close-packed (hcp) and face-centered-cubic (fcc) lattices have been determined by utilizing an iterative approach that uses a configurational cluster expansion method, Monte Carlo search algorithm, and density functional theory (DFT) calculations. Based on 64-atom models, it is shown that the most stable phases of the Mg-Zn binary alloy under ambient condition are $MgZn_3$, $Mg_{19}Zn_{45}$, $MgZn$, and $Mg_{34}Zn_{30}$ for the hcp lattice, and $MgZn_3$ and $MgZn$ for the fcc lattice, whereas the Al-Zn binary is energetically unfavorable throughout the entire composition range for both the hcp and fcc lattice symmetries under all pressure conditions. By applying an isotropic pressure in the hcp lattice, $Mg_{19}Zn_{45}$ turns into an unstable phase at $P \approx 10$ GPa, a new stable phase $Mg_3Zn$ appears at $P \gtrsim 20$ GPa, and $Mg_{34}Zn_{30}$ becomes unstable for $P \gtrsim 30$ GPa. For the fcc lattice, the $Mg_3Zn$ phase weakly touches the convex hull at $P \gtrsim 20$ GPa while the other stable phases remain intact up to $\approx 120$ GPa. Furthermore, making use of the obtained DFT results, the bulk modulus has been computed for several compositions up to pressure values on the order of $\approx 120$ GPa. The findings suggest that one can switch between Mg-rich and Zn-rich early-stage clusters simply by applying external pressure. Zn-rich alloys and precipitates are more favorable in terms of stiffness and stability against external deformation.

## I. INTRODUCTION

The controlled creation of alloys is an attractive research field from both theoretical and experimental standpoints [1–3]. An alloy system comprises numerous charged particles that interact with each other and make a highly complicated interacting many-body platform. As is evident, this level of complexity makes accurate theoretical studies of such systems quite challenging, and therefore multiple approximations with today's computers have to be incorporated [4–14]. The interplay of the quantum mechanical interactions and the specific spatial ordering of different atoms, forming an alloy, determines the macroscopic properties of alloys, and this has served as a unique platform for testing and developing various theoretical approaches [4,5,7,15–17]. On the other hand, the detailed atomistic level insight from theoretical studies may provide useful information for synthesizing alloys in experiments with boosted specific properties [14,18–21]. Prominent examples can be found in aluminum alloys that play increasingly crucial roles in various industrial products [5,8–12,22–25].

One of the main goals of alloying matrices is to obtain the most lightweight and high-strength alloys that can be extensively used in aircraft industries, modern trains and vehicles, and so forth. The central mechanisms for enhancing the strength of aluminum is to produce uniform distributions of nucleated precipitates and solid microstructures in the aluminum matrix with different solute elements such as Zn, Mg, Si, Cu, Mn, and Cr [26–35]. Among them, however, Zn and Mg have demonstrated to be the most effective additives

to help the growth of precipitates from solute clusters, thus enhancing the strength and hardness of the Al matrix through generating high resistance against dislocation motion and damage. For example, a recent experiment has demonstrated that a cyclic deformation of an Al alloy at room temperature facilitates a diffusion of solid solute clusters and eventually generates a matrix with uniformly close packed precipitates that increase the material strength and elongation properties. The advantages of this method compared to conventional temperature-aging approaches are (i) a shorter processing time and (ii) a more uniformly distributed microstructure with no precipitate-free zones [36]. Also, it has been experimentally observed that several phases of precipitates can develop in Mg-Zn and Al-Zn-Mg alloys, including MgZn, monoclinic $Mg_4Zn_7$, $\eta$-$MgZn_2$, $\beta$-$MgZn_2$ with hexagonal symmetry, $Mg_2Zn_3$, and $Mg_2Zn_{11}$ [37–43]. Recent systematic investigations have demonstrated that the morphology and structural evolution of precipitates in Mg alloys are closely linked to their internal sub-unit-cell arrangements, the aspect ratio of precipitates, misfit strains, and their interaction with matrix interfaces [37,44–46].

Despite the extensive attention that aluminum alloys have received so far, only limited studies have been performed for investigating their fundamental properties when subject to tension from atomistic-level first principles [47,48]. The findings of such high-end rigorous studies not only can be used as guidelines for future experiments but they also can be employed as benchmark tests for computationally less expensive approaches (such as effective potential methods

[4,5,7,15,16] which are crucial for molecular dynamics simulations or phase field approximations). Hence, these results can serve in developing reliable multiscale models for providing better insights into closer-to-realistic sample sizes. Also, there are several magnesium and zinc rich alloys that, respectively, contain Al/Zn and Al/Mg elements as the most effective additions to improve their hardness. Therefore, it is of fundamental interest to study these alloys within the entire composition range. In order to provide insights for the Al-Mg-Zn alloys, one first needs to study the properties of the Al-Mg, Mg-Zn, and Al-Zn binaries, which comprise the boundaries of the Al-Mg-Zn trinary composition diagram. The properties of the Al-Mg binary have already been studied in previous works [8,9], and thus, we focus here on the Mg-Zn and Al-Zn binaries only.

In this work, we employ an iterative combination of a cluster expansion (CE) method, Monte Carlo (MC) simulations, and density functional theory (DFT) calculations to exhaustively search and find the stable phases of the Mg-Zn and Al-Zn binary alloys, starting from both hexagonal-close-packed (hcp) and face-centered-cubic (fcc) lattice symmetries. Our theoretical results show that the stable phases of the Mg-Zn binary are mixture and layered configurations of the two elements in the hcp lattice, and they are in line with experimental observations where $MgZn_2$, $Mg_4Zn_7$, and $MgZn$ compositions with hexagonal symmetry have been found as the most stable phases. For the fcc lattice, we find layered geometrical motives emerging for $MgZn$ and higher Mg concentrations. The Al-Zn binary turns out to be energetically unfavorable on both the hcp and fcc lattice symmetries under all pressure conditions studied, which indicates a segregation behavior. Although the free energies of Mg-rich compositions are lower than those of Zn-rich ones for the Mg-Zn binary, the presence of an external pressure can revert the situation such that Mg-rich alloys become unstable. The analysis of bulk modulus for several compositions illustrates that Zn-rich compositions have the largest bulk modulus and they are more resistant to external deformation. These findings suggest that by applying an appropriate pressure to early-stage clusters of the Mg-Zn binary, one can control the type of the precipitate clusters (being either Zn-rich or Mg-rich solid solutions), and thus tune the absolute hardness of the entire matrix.

The article is organized as follows. In Sec. II, we briefly discuss and present the theoretical framework used in order to find the energetically favorable phases of binary alloys. In Sec. III, we present our main findings and a detailed description of the results. Finally, in Sec. IV, we present concluding remarks.

## II. METHODS

In this section, we describe the theoretical framework and computational details.

### A. Density functional theory calculations

The first-principles calculations based on the density functional theory of electronic structure were performed using the GPAW code [49,50]. The interaction between ions (nuclei + core electrons) and valence electrons was described by using the projector augmented wave method. The gradient-corrected functional by Perdew-Burke-Ernzerhof (PBE) was employed for the exchange correlation energy, the plane-wave cutoff for kinetic energy was set to 600 eV, and the number of electronic bands was chosen as 120% (corresponding to 20% unoccupied). Furthermore, we have used 3.5 **k** points per $\text{Å}^{-1}$ in order to grid **k** space on the basis of the Monkhorst-Pack scheme. In order to produce consistent data, we have kept fixed all the above-mentioned parameters throughout all DFT calculations. The parameter values were chosen based on extensive convergence and consistency tests, and they provide a balance between convergence and good accuracy in all calculations. We have exploited the "fast inertial relaxation engine" and ExpCellFilter modules available in the atomistic simulation environment package [51] to relax the atomic positions in a given structure under isotropic pressure through self-consistent loops until the residual forces on each atom become less than 0.07 eV/Å. We have cross-checked our DFT calculations for selected compositions with tighter convergence criteria and found no changes in the resulting convex hull. In total, 861 individual configurations of 64 atoms were DFT-optimized based on these specifications at zero pressure, and the most stable configurations at the convex hull were subjected to additional pressure calculations.

### B. Cluster expansion model

The cluster expansion (CE) model is a generic approach that can describe multicomponent systems through trainable parameters. The main objective is thus to develop CE models with the ability to predict configurational properties with high accuracy and much less computational cost than for DFT [17,52–58]. In this work, CE provides an effective Hamiltonian, describing the configurational energy of Mg-Zn and Al-Zn alloys. Each element atom type is represented by a pseudospin $\tau_\alpha$ with an effective cluster interaction $E_\alpha$ at a configurational ordering $\alpha$ (specific order of atoms in a given composition). Thus, with this approach, we can expand and express the energy of a given configuration by

$$E = E_0 + \sum_i E_i \tau_i + \sum_{i,j} E_{ij} \tau_i \tau_j + \sum_{i,j,k} E_{ijk} \tau_i \tau_j \tau_k + \cdots .$$
(1)

The effective cluster interactions $E_\alpha$ are unknown coefficients. The main task is to train the above expansion to DFT data (training set) and to find the best values for $E_\alpha$ in a truncated series to describe the configurational energy accurately. The accuracy of CE predictions depends crucially on several ingredients: The number of structures in the data set, how the structures are chosen, the number of effective correlation functions (how many terms the expansion possesses), and the correlation functions used for fitting to the data set. The method we chose to find the best truncated series is the minimization of the leave-one-out cross validation (CV) score through the least absolute shrinkage and selection operator (LASSO), i.e.,

$$\min_\alpha \left\{ \sum_{n=1}^{N} \left( E_{\text{DFT}}^n - E_{\text{CE}}^n \right)^2 + \alpha \sum_\alpha |E_\alpha| \right\},$$
(2)

in which $N$ is equal to the number of configurations evaluated by DFT calculations, $E_{DFT}^n$ represents the energy of the $n$th structure predicted by DFT, and $E_{CE}^n$ is the prediction made by CE. The second term in Eq. (2) is a cost function, where the term $\alpha$ regularizes the coefficients such that it imposes a penalty on coefficients with large values and helps in reducing overfitting. To construct CE models, we have employed the open source PYTHON modules in the CLEASE software [54].

### C. Monte Carlo simulations

The configuration space of 64-atom model structures for Mg-Zn and Al-Zn alloys contains a large number of unique configurations, made of various combinations of the considered elements within the entire composition range. Therefore, it is not feasible to evaluate all possible configurations in the configuration space using DFT calculations. In order to effectively search the configuration space and to find the energetically most favorable configurations, we have used the Metropolis algorithm and Monte Carlo simulations [59]. In short, one shuffles the list of atoms in a given configuration and calculates the energy difference between the new $j$ and old $i$ configuration: $\Delta E = E_j - E_i$. Next, one picks up a random number $r$ and defines a probability for accepting the new configuration $j$ together with a simulated annealing algorithm at a temperature $T$ as follows:

$$r < \exp\left\{ -\gamma \frac{\Delta E}{k_B T} \right\}. \quad (3)$$

Here, $k_B$ is the Boltzmann constant and $\gamma$ is a parameter that controls the acceptance rate of new structures. Depending on the number of possibilities available within the configuration space, one produces a sufficient number of random structures by swapping atoms in each Metropolis step and then increases $\gamma$ slowly from highly small values (equivalent to a high acceptance rate) to large values of $\gamma$ where the acceptance rate of new structures become highly suppressed [59]. Note that at a low enough temperature regime where $k_B T \to 0$, one can remove $\gamma$ and use $k_B T$ as the controlling parameter for the acceptance rate by varying the temperature exponentially from high (equivalent to small values for $\gamma$) to low enough values (equivalent to large values for $\gamma$).

### III. RESULTS AND DISCUSSION

#### A. Atomic structure, energetics, and the effect of pressure

A CE model is inevitably tied to the elements in question and lattice symmetry, making it almost impractical to train only one model for a set of alloys with different lattice symmetries. Therefore, we have trained several CE models for each alloy system with a specific lattice structure. To find the energetically most favorable structures for Mg-Zn and Al-Zn binaries, we have chosen the following strategy which is tedious but reliable: (i) We produce a database of 40 randomly generated unique structures. (ii) Considering the parameters described in Sec. II A, we perform DFT calculations (always requiring geometry and unit cell optimization) for structures generated in the previous stage. (iii) We construct more than 50 CE models as explained in Sec. II B by varying the maximum diameter of clusters. (iv) By selecting CE models

possessing CV scores (prediction error with respect to DFT results) less than 10 meV, we generate new unique low-energy structures and add them to the database if not already existing. (v) Extracting these new unique structures, we perform DFT calculations and repeat stages (iii) to (v) until new CE models are not able to add new unique structures into the database, and the procedure reaches convergence.

We have carried out the above steps for the Mg-Zn and Al-Zn binaries on both the hcp and fcc lattice symmetries and used identical fitting procedures for the surrogate CE models. In the following, we have neglected vibrational effects at finite temperature. For the $2 \times 2 \times 2$, $3 \times 3 \times 3$, and $4 \times 4 \times 4$ unit cell structures the concentration of elements changes by steps of 12.50%, 3.7037%, and 1.5625%, respectively. Therefore, the last case (64 atoms) with the smallest step allows for exploring the full range of concentrations more precisely. We remark here that the structures have *initially* an ideal hcp/fcc lattice symmetry but the DFT optimization (geometry, cell) results in small deviations both in terms of symmetry and individual atomic positions. This means that the DFT total energies present in our CE training database correspond to fully optimized configurations.

In order to compare different compositions based on the (free) energies calculated by DFT, we define the formation energy of a binary $\mathcal{AB}$, regardless of its lattice symmetry, as follows:

$$H[\mathcal{A}_x \mathcal{B}_{1-x}] = E[\mathcal{A}_x \mathcal{B}_{1-x}] - (1-x)E[\mathcal{B}] - xE[\mathcal{A}], \quad (4)$$

where $x$ is the concentration of the $\mathcal{A}$ element and $E[\mathcal{A}_x \mathcal{B}_{1-x}]$ is the free energy of composition $\mathcal{A}_x \mathcal{B}_{1-x}$. Also $E[\mathcal{B}]$ and $E[\mathcal{A}]$ are the free energies of pure elements $\mathcal{A}$ and $\mathcal{B}$, respectively. Note that we assume here zero temperature where potential energy, configurational energy, and free energy are the same. At finite-temperature values, however, one should differentiate when using these terminologies.

Figure 1 summarizes the results of the above strategy for the Mg-Zn binary in the hcp lattice. To reach convergence as described above, this process has demanded gradually adding and calculating the configurational energies of 402 unique structures from first principles. The plot exhibits the formation energy of these 402 structures, calculated by Eq. (4), as a function of Mg concentration. The energetically most favorable structures (compositions) are those with energies touching the convex hull (black curve). To make these more visible, we have marked them by solid red circles while other structures close to the convex hull are marked by green circles.

We find that Zn, $MgZn_3$, $Mg_{19}Zn_{45}$, $MgZn$, $Mg_{34}Zn_{30}$, and Mg construct the convex hull and are the most favorable compounds for the hcp lattice. We also show four other compounds, i.e., $Mg_{15}Zn_{49}$, $Mg_{17}Zn_{47}$, $Mg_{21}Zn_{43}$, and $Mg_3Zn$, that are close to the convex hull. The free energies of these configurations are summarized in Table I. The corresponding real-space $4 \times 4 \times 4$ configurations are displayed on the right-hand side of Fig. 1, and they show gradual changes in site occupations. The prominent feature of these structures is that they show a strong mixing of Mg and Zn in the hcp lattice symmetry over the entire composition range. The corresponding $5 \times 5 \times 5$ extended supercells are presented in Fig. 9 in the Appendix.
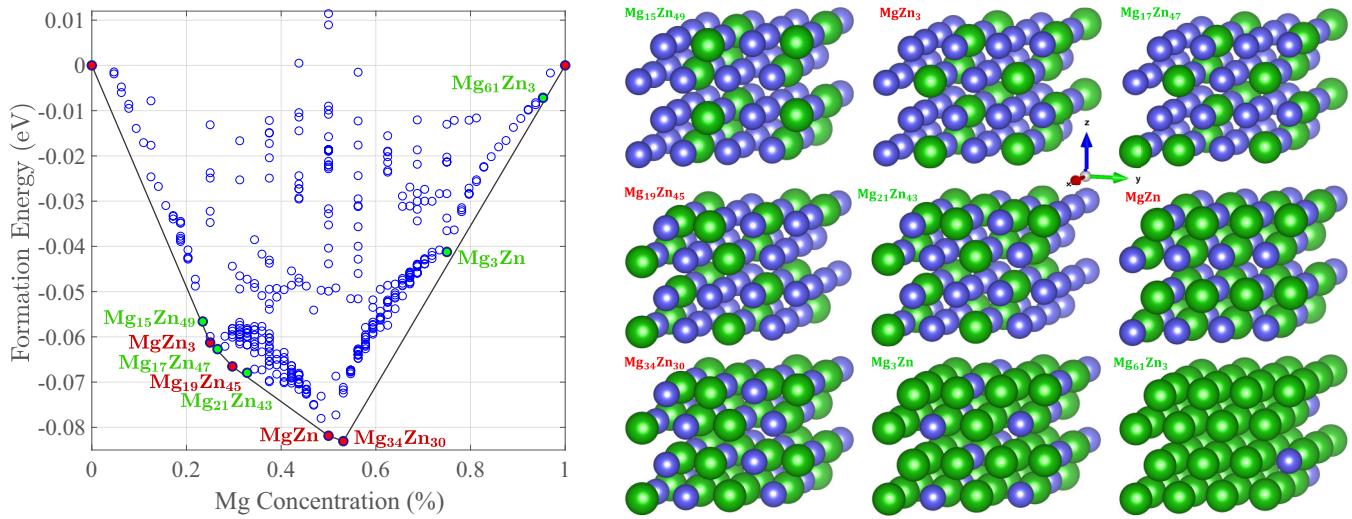
FIG. 1. Left: The convex hull of the Mg-Zn binary in the hcp lattice. To obtain the convex hull, we have performed DFT calculations for 402 individual configurations predicted by an iterative use of DFT, CE method, and Monte Carlo simulations. The convex hull illustrates that $MgZn_3$, $Mg_{19}Zn_{45}$, MgZn, and $Mg_{34}Zn_{30}$ (marked by the solid red circles) are stable phases. We have also marked other compositions that are close to the convex hull by the solid green circles. Right: 64-atom hcp configurations ($4 \times 4 \times 4$ structures) corresponding to the phases marked by the solid circles in the left panel. The green and blue spheres stand for Mg and Zn atoms, respectively.

Note that since we are restricted by $4 \times 4 \times 4$ structures due to computational limitations in DFT calculations, we are able to span the concentration range only by steps of 1.5625%. Therefore, there may exist other energetically favorable compounds close to the convex hull (namely, they fall into regions that are only explorable through larger atomic models). Nevertheless, the step of 1.5625% is small enough to allow us to provide an overview of the convex hull for binary alloys. The stable phases with hexagonal symmetries in experiment are $Mg_2Zn_3$, $Mg_2Zn_{11}$, $MgZn_2$, $Mg_4Zn_7$, and MgZn [37–43]. The last case was also explored and confirmed in our results above. The ratios of the other two compositions, 1:2 and 4:7, do not match exactly with the $4 \times 4 \times 4$ structures considered in this study, but the predicted phase $Mg_{21}Zn_{43}$ lends support also for these experimental observations [37–43].

Another limitation considers the (possible) structural transition upon alloying or applying pressure. In this case, the searchable configuration space would considerably increase and include numerous new possibilities. We postpone addressing these interesting topics to our future works, and thus assume here that no structural transitions beyond the hcp/fcc will take place under alloying and/or the application of pressure. Note that as close-packed structures the hcp and fcc lattices have the largest coordination number, i.e., 12 (sphere packing efficiency of 0.74), and it does not seem plausible that other lattice structures (such as body-centered cubic) would emerge as a result of applying pressure.

Next, we study the Mg-Zn binary with the fcc lattice symmetry. As bulk materials, Mg and Zn have the hcp lattice symmetry whereas Al exists as the fcc lattice symmetry. However, as fully confirmed by experiments, the solid solutes and clusters in Al-dominated matrices tend to mimic the lattice symmetry of bulk Al and develop fcc-like sublattices. Therefore, in order to understand the properties of the Mg-Zn solid clusters in the Al-dominated matrices one needs to study this binary with the fcc symmetry as well. Figure 2(a) shows the

normalized free energy of 232 unique structures as a function of concentration. The fcc structures have been systemically collected in the DFT database as described above for the hcp case. Figure 2(a) shows the normalized free energy and Fig. 2(b) exhibits the associated formation energy obtained by Eq. (4). Note that the hcp structures display exactly the same trend (not shown) as Fig. 2(a) since the energy differences between the fcc and hcp configurations are very small. For the fcc lattice symmetry, the convex hull is made by Zn, $MgZn_3$, MgZn, and Mg marked by solid red circles. We have also marked $Mg_6Zn_{58}$ and $Mg_3Zn$ (by green solid circles) that have energies closer to the convex hull than other compounds. The normalized free energies of these compounds (shown by blue circles) are summarized in Table II. The corresponding real-space $4 \times 4 \times 4$ configurations are shown on the right-hand side of Fig. 2. Interestingly, unlike for the hcp compounds, $Mg_6Zn_{58}$ and $MgZn_3$ suggest a full mixture of Mg and Zn atoms from 0% to 30% magnesium, while the stable MgZn phase and $Mg_3Zn$ display that compositions containing more than 50% of Mg tend to create layered structures. In order to ease the visibility of the mixture and layered compositions, we present visualizations of the $5 \times 5 \times 5$ extended cells in Fig. 9 in the Appendix.

We have carried out the same computational procedure as above for the Al-Zn binary. Figure 3(a) shows the formation energy as a function of Al concentration for 164 unique structures, gradually collected through iterating the loop between the stages (i) and (v). The corresponding free energies are presented in Fig. 10 in the Appendix. Here we have considered both $3 \times 3 \times 3$ and $4 \times 4 \times 4$ structures with the fcc lattice symmetry. The formation energy is either positive or takes very small negative values throughout the full composition range. The overall positive formation energy indicates that the Al-Zn binary tends to segregate always. This is confirmed by the atomic configurations of the lowest-energy structures (not shown) which show a strong segregation of Al and
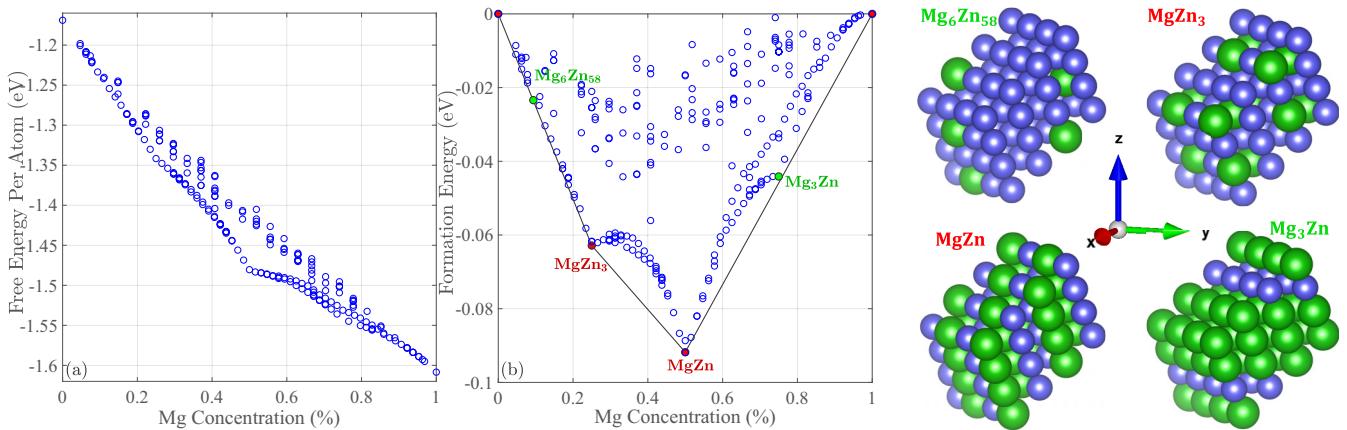
FIG. 2. The Mg-Zn binary with the fcc lattice symmetry. (a) Normalized free energy of 232 configurations as a function of Mg concentration (in percent). (b) The convex hull of these 232 unique configurations with $4 \times 4 \times 4$ unit cell structures containing 64 atoms. The stable phases are $MgZn_3$ and $MgZn$ (marked by the solid red circles), whereas $Mg_6Zn_{58}$ and $Mg_3Zn$ (marked by the solid green circles) are close to the convex hull. The corresponding atomic structures are shown on the right side. The green and blue spheres stand for Mg and Zn atoms, respectively.

Zn. To provide further insight for this binary, we show in Fig. 3(b) the formation energy of the Al-Zn binary for the hcp lattice. Clearly, Al and Zn prefer to separate as for the fcc lattice symmetry. We also present results for the isotropic pressures of 40 GPa and 80 GPa in the hcp case. Introducing a nonzero pressure results in a stronger positive formation
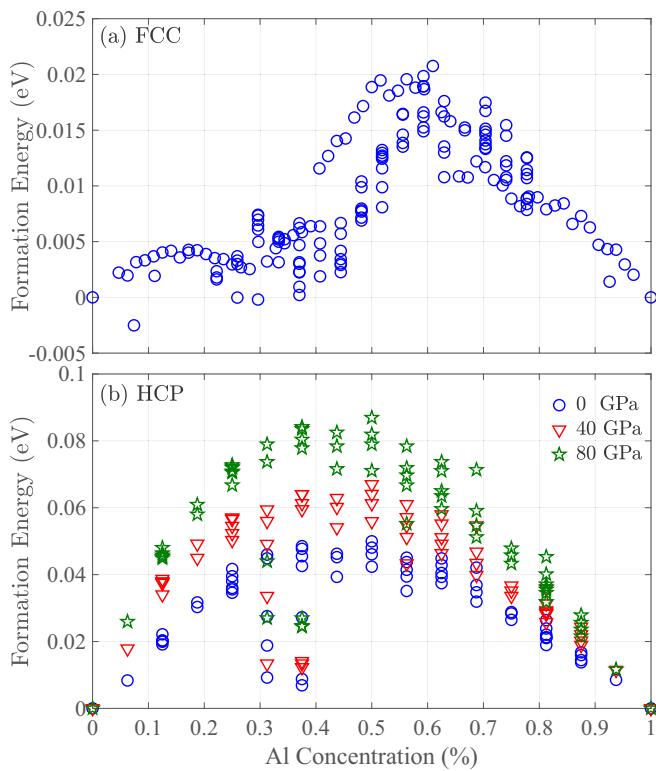


FIG. 3. Formation energy of unique configurations of the Al-Zn binary as a function of Al concentration. (a) The fcc lattice with 163 unique configurations ($3 \times 3 \times 3$ and $4 \times 4 \times 4$ structures). The external pressure is set to zero. (b) The hcp lattice and 64 unique configurations under external pressure: $P = 0, 40, 80$ GPa.

energy, and thus, it is unable to assist in mixing of the Al and Zn elements. Note that as pure Al and Zn belong to the fcc and hcp lattice symmetries [60], respectively, the final segregated compositions might be mixtures of these two symmetries. Nevertheless, in Al-rich and Zn-rich alloys, one can expect that the leading lattice symmetry is dictated by the fcc and hcp symmetries, respectively.

Having determined the stable phases of the Mg-Zn binary on the hcp and fcc lattices, we now subject these compounds (together with those nearby the convex hull) to an external pressure. Figure 4(a) shows the normalized free energy of 11 compounds against externally applied isotropic pressure from 0 to 120 GPa. Under ambient conditions, bulk Mg and Zn have the lowest and highest free energy, respectively, and the other compounds are located between these two limits. By applying the external pressure, the free energy of all compounds increases and in high-pressure regions, larger than 80 GPa, the free energy becomes positive, limiting the formation of solid state compounds. Figure 4(a) illustrates that although Mg-rich compounds are more stable in the low-pressure regime, they turn unstable faster than those with a higher concentration of Zn and there is a crossover at 30 GPa. Correspondingly, the Zn-rich compounds show more stability under pressure, which can be used as a control knob for switching between the two types of alloys. Also, this finding can be expanded to large enough precipitates of these elements: By applying pressure to an Al matrix where Mg and Zn solute atoms form solid clusters, one may be able to externally control the type of the clusters to be either Mg-rich or Zn-rich. Figure 4(b) shows the normalized volume of each compound against the applied isotropic pressure. Obviously, bulk Mg and Zn exhibit the highest and lowest volume reduction, respectively, and the rest are located between these two limits. The percentage of volume reduction confirms the higher stability of Zn-rich compounds.

One important quantity that we can calculate now is the bulk modulus $B_0$ which measures the stiffness of a material against elastic deformation when subject to an external pressure. To this end, we make use of the Birch-Murnaghan
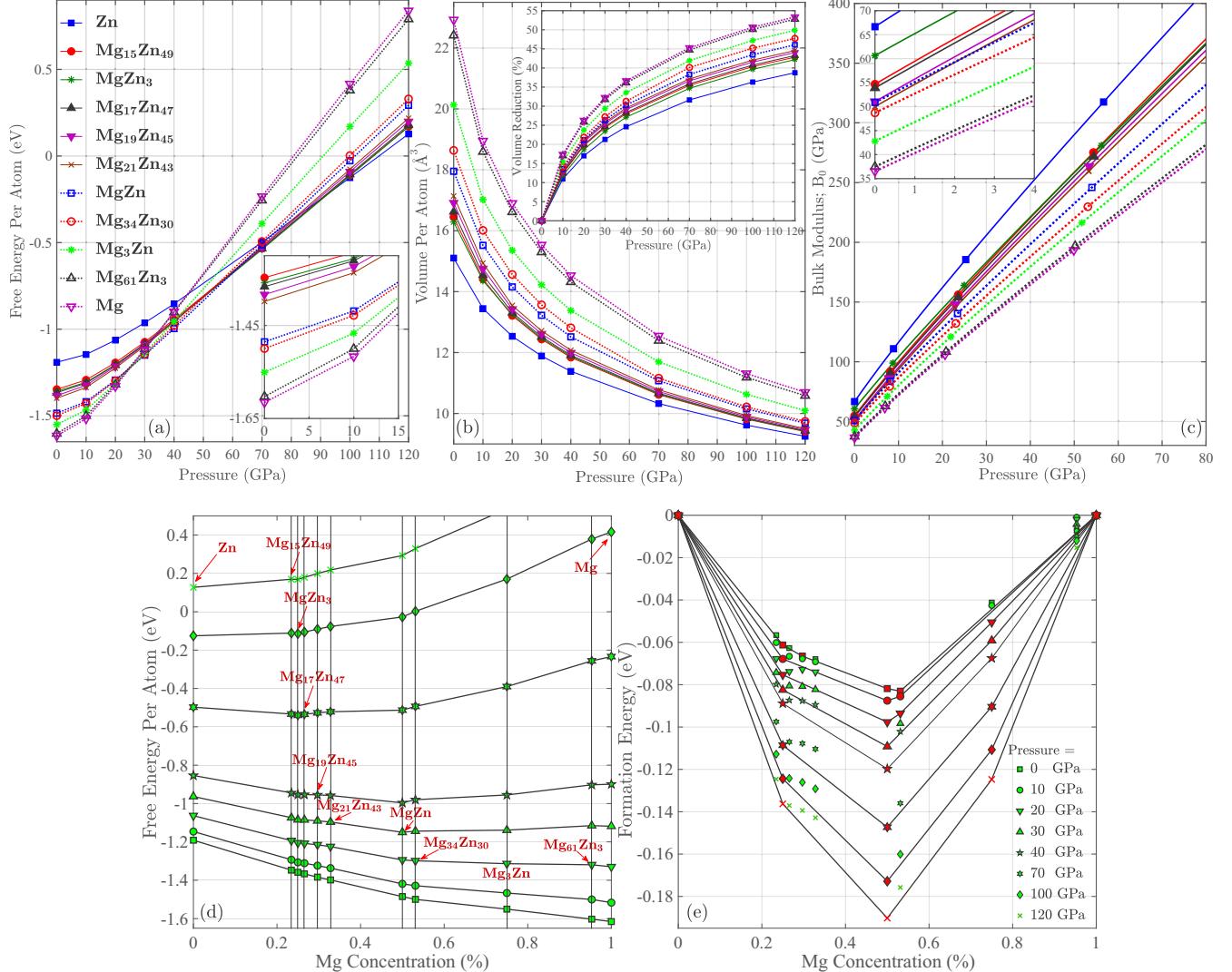
FIG. 4. The Mg-Zn binary with the hcp lattice symmetry. (a) The free energy of marked phases in the convex hull, normalized by the number of atoms in supercell, as a function of applied isotropic pressure from 0 GPa to 120 GPa. (b) Change in the normalized volume of different compounds when applying the isotropic pressure. The inset panel shows the percentage of volume reduction due to the exerted pressure. (c) Bulk modulus, $B_0$, of different compounds under pressure. The inset panel is a zoomed-in shot of the bulk modulus restricted to low pressures (from 0 GPa to 5 GPa). (d) Normalized free energy of different compositions as a function of Mg concentration (in percent) at various values of the isotropic external pressure: $P = 0, 10, 20, 30, 40, 70, 100, 120$ GPa. (e) Variation of convex hull and the evolution of the stable phases by increasing the external pressure. The stable phases are marked by red color, while the remaining compounds are shown by green.

empirical equation of state for pressure as a function of volume:

$$P(V)$$
$$= \frac{3B_0}{2}\left\{1 + \frac{3(B_0' - 4)}{4}\left[\left(\frac{V_0}{V}\right)^{\frac{2}{3}} - 1\right]\right\}\left\{\left(\frac{V_0}{V}\right)^{\frac{7}{3}} - \left(\frac{V_0}{V}\right)^{\frac{5}{3}}\right\},$$
(5)

in which $B_0$ is the bulk modulus, $B_0'$ is the derivative of the bulk modulus with respect to pressure, $V_0$ is the volume at zero pressure, $V$ is the volume, and $P$ is the pressure. Also, the bulk modulus is closely linked to the speed of sound (mechanical

waves) and the energy stored in a solid system, which is given by

$$B_0 = -V\left(\frac{\partial P}{\partial V}\right).$$
(6)

To evaluate Eq. (6), we first find the set of parameter values that fits Eq. (5) into our DFT data such that we obtain $P(V)$ numerically, and thus $B_0$ can be evaluated. Figure 4(c) shows the bulk modulus of the Mg-Zn compounds. The calculated bulk moduli of the elemental Mg and Zn are in good agreement with those reported values in experiments. The calculated and measured $B_0$ are summarized in Table III. The bulk moduli of the Mg-Zn compounds are located between those of bulk
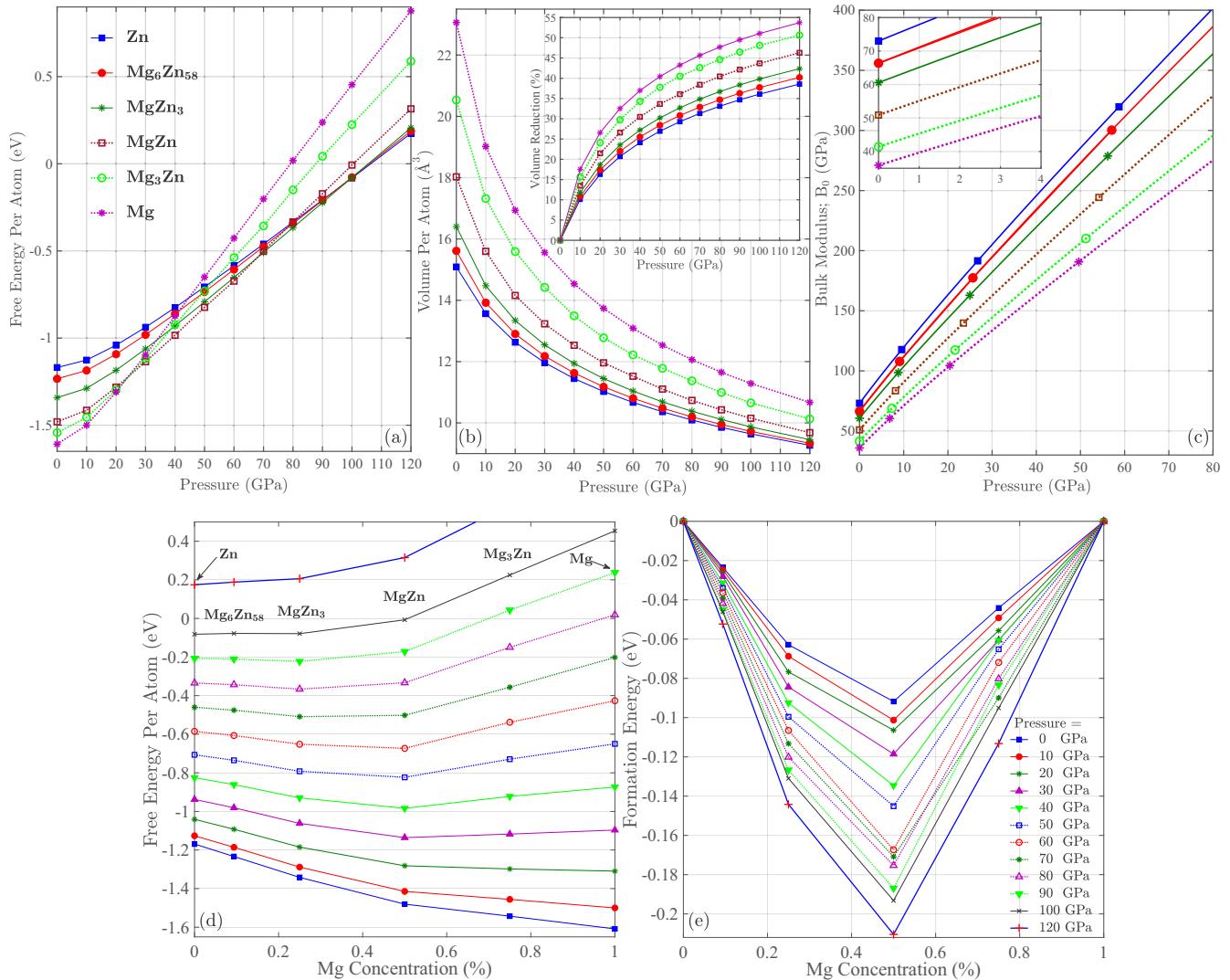
FIG. 5. The Mg-Zn binary with the fcc lattice symmetry. (a) Normalized free energy of the Mg-Zn compositions as a function of the externally applied isotropic pressure from 0 GPa to 120 GPa with the step of 10 GPa. (b) Normalized volume of the compounds as a function of pressure. The inset panel exhibits the volume reduction of each compound as a function of pressure. (c) Bulk modulus as a function of pressure. The inset shows a zoomed-in shot of the bulk modulus at low pressures. (d) Normalized free energy as a function Mg concentration. (e) Formation energy of the Mg-Zn binary phases.

Zn and Mg from top to bottom, respectively. Clearly, we can conclude that Zn-rich compounds are stiffer than those with a high concentration of Mg.

In order to evaluate the stability of these compounds subject to isotropic pressure, we show their normalized free energy values as a function of Mg concentration in Fig. 4(d) at several pressures. The associated convex hulls are presented in Fig. 4(e). As evidenced above based on the bulk moduli, the free energy of bulk Mg [Fig. 4(d)] has the largest variation. To make this clearer, we have marked stable phases, touching the convex hull, by solid red symbols, while those compounds away from the convex hull are displayed in green. We find that MgZn$_3$ and MgZn show stability in the entire interval of the applied pressure. Interestingly, we see that Mg$_{19}$Zn$_{45}$, which is a stable phase at zero pressure, becomes unstable at larger pressure values than 10 GPa. Similarly, Mg$_{34}$Zn$_{30}$ becomes unstable at pressures higher than 40 GPa. Remarkably, Mg$_3$Zn becomes more stable at pressures higher than 20 GPa

as it not only touches the convex hull but also comprises a new minimum above 70 GPa.

Figure 5 is the fcc counterpart of Fig. 4 showing the effect of pressure on the stable phases Mg$_6$Zn$_{58}$, MgZn$_3$, MgZn, and Mg$_3$Zn. The normalized free energies reside between those of bulk Zn and Mg from zero pressure up to 30 GPa. Similarly to the hcp case, the free energy changes its sign above 80 GPa, starting from bulk Mg. At 30 GPa, MgZn crosses with bulk Mg and becomes the lowest-energy compound. At 80 GPa, MgZn$_3$ has the lowest free energy, and bulk Mg and bulk Zn change their places as the upper/lower boundary above 100 GPa. Note that for both the hcp and fcc lattices, pressure-controlled alloying becomes possible around 30 GPa, in particular at pressure values larger than 40 GPa. Figure 5(b) illustrates the normalized volume and the results are very similar to those for the hcp compounds in Fig. 4(b). We conclude from this that Zn-rich alloys are less sensitive to changes in pressure. For the bulk modulus [Fig. 5(c)], as
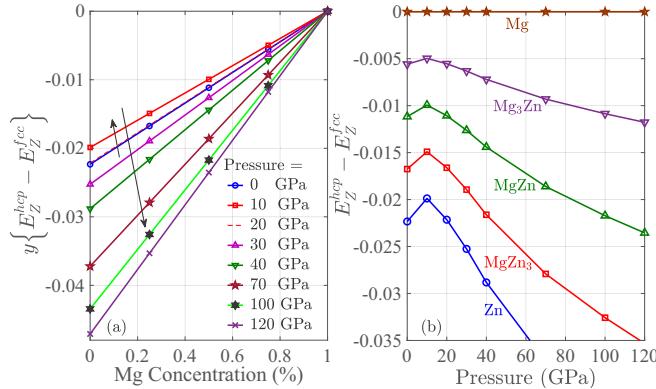
FIG. 6. Structural energy difference of the Mg-Zn alloys under the isotropic external pressure. The vertical axis is in units of energy (eV).

before, bulk Zn and bulk Mg exhibit the highest and lowest $B_0$ values, respectively. The bulk moduli of Mg on the hcp compounds and fcc lattices are almost the same [Figs. 4(c) and 5(c), insets]. However, the bulk modulus of Zn enhances by almost 15% by the lattice change. Hence, our analysis demonstrates that Zn-rich alloys with the fcc lattice symmetry are more favorable in terms of hardness and stability against external deformation.

In Fig. 5(d), we plot the normalized free energy as a function of Mg concentration and pressure, and Fig. 5(e) displays the associated convex hull. Here, $MgZn_3$ and $MgZn$ are stable throughout the pressure interval 0–120 GPa, while $Mg_6Zn_{58}$ stays close to the convex hull. $Mg_3Zn$ touches the convex hull above 20 GPa but does not introduce a new minimum. This differs from the hcp case where $Mg_3Zn$ becomes stable as pressure increases. Therefore, we can conclude that $Mg_3Zn$ with the fcc lattice symmetry has a limited stability when subject to pressure.

Finally, let us consider a situation where the Mg-Zn binary can be a mixture of the hcp and fcc lattices. We calculate the mixing enthalpy and obtain the structural energy differences as follows:

$$\Delta H^{\text{hcp}}[M_x Z_y] = E^{\text{hcp}}[M_x Z_y] - y E_Z^{\text{fcc}} - x E_M^{\text{hcp}}, \quad (7a)$$

$$\Delta H^{\text{fcc}}[M_x Z_y] = E^{\text{fcc}}[M_x Z_y] - y E_Z^{\text{hcp}} - x E_M^{\text{fcc}}, \quad (7b)$$

where $y \equiv 1 - x$ and $E_{M,Z}^{\text{hcp,fcc}}$ are the energies of Mg and Zn on the hcp and fcc lattices. If we now add and subtract $y E_Z^{\text{hcp}}$ and $y E_Z^{\text{fcc}}$ on the right-hand sides of the two equations, respectively, we find

$$\Delta H^{\text{hcp}}[M_x Z_y] = H^{\text{hcp}}[M_x Z_y] + y\{E_Z^{\text{hcp}} - E_Z^{\text{fcc}}\}, \quad (8a)$$

$$\Delta H^{\text{fcc}}[M_x Z_y] = H^{\text{fcc}}[M_x Z_y] + y\{E_Z^{\text{fcc}} - E_Z^{\text{hcp}}\}, \quad (8b)$$

where $H^{\text{hcp,fcc}}[M_x Z_y]$ is the isostructural mixing enthalpy on the hcp and fcc lattices, given by Eq. (4). Thus, the last terms in the above equations provide the contribution of the structural energy difference in the Mg-Zn alloys. We have plotted this quantity for Zn, $MgZn_3$, MgZn, $Mg_3Zn$, and Mg as a function of pressure in Fig. 6. The structural energy difference is very small, indicating that Mg and Zn can acquire the fcc phase with a small energy cost. When we increase
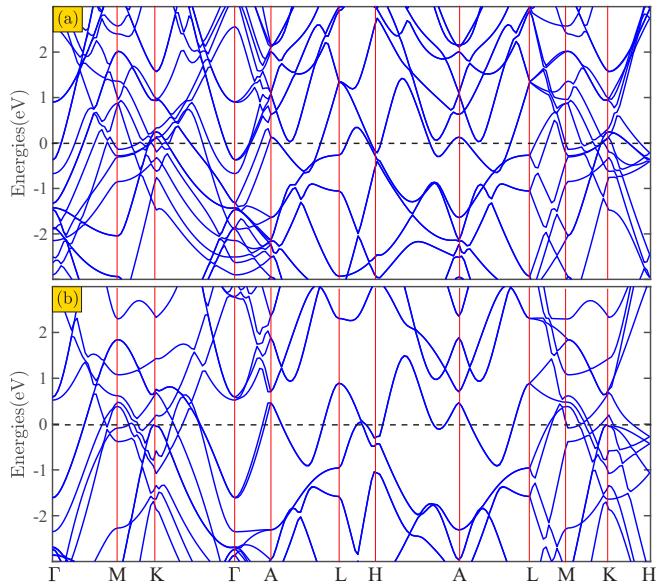


FIG. 7. Electronic band structure of the MgZn with the hcp symmetry ($2 \times 2 \times 2$ unit cell) along the high-symmetry lines. The vertical lines exhibit the location of high-symmetry points. The Fermi level is shifted to zero energy. (a) Ambient condition ($P = 0$ GPa); the normalized volume per atom is 18.3981 Å. (b) $P = 120$ GPa; the normalized volume per atom is 9.8069 Å.

the pressure the structural energy difference first increases at 10 GPa and then decreases while remaining negative the whole time, demonstrating that the hcp lattice remains always energetically preferable. These findings can be confirmed by comparing the free energy values in Tables I and II. We note here that according to the experimental observations, large enough precipitates develop hexagonal lattice symmetry under ambient conditions [37,38,41–43].

### B. Electronic band structure and density of states

DFT calculations include explicit information on the electronic structure for all configurations sampled in this study. Here, we present the density of states and band structure for the MgZn compound and hcp lattice symmetry, which is one of the lowest-energy configurations located at the convex hull (see Fig. 1). In order to find out how the applied pressure can influence the electronic properties, we have systematically scaled down the unit cell volume and plotted the associated band structure, total density of states (TDOS), and projected density of states (PDOS). Figure 7 illustrates the band structure along the high-symmetry lines. We have considered two different normalized volumes 18.3981 Å and 9.8069 Å in Figs. 7(a) and 7(b) corresponding to $P = 0$ and $P = 120$ GPa, respectively. The band energies are shifted such that the zero energy corresponds to the Fermi level. The effect of pressure is evident around the Fermi level where there are fewer bands at high pressure. Further, by selecting the symmetry points $\Gamma$ and $A$ as examples, one can see that there are bands which have been pushed at lower energies in the valence band.
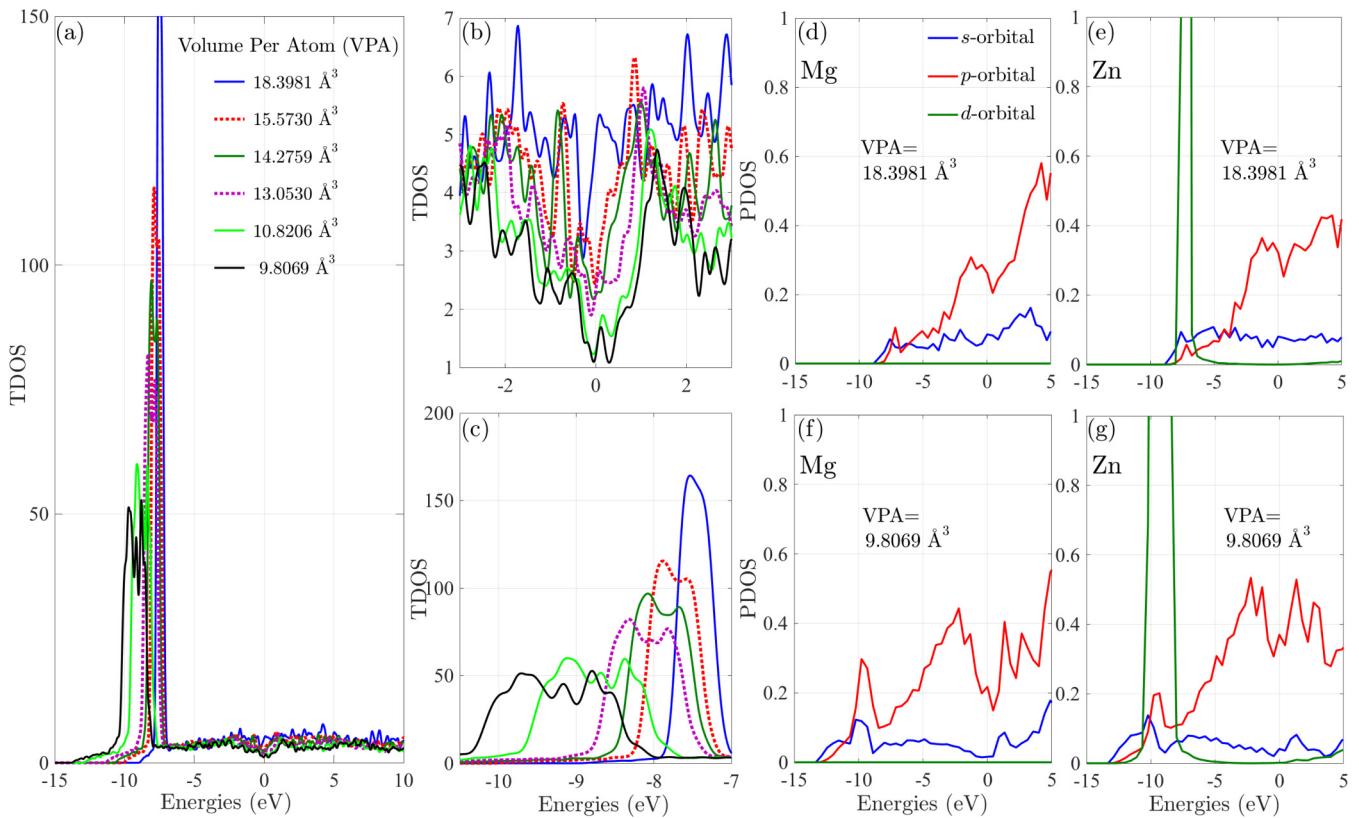
FIG. 8. Total and projected density of electronic states (TDOS/PDOS) of MgZn with the hcp symmetry as a function of energy. The Fermi level is shifted to zero energy. TDOS is plotted for six values of volume per atom: 18.3981 $\text{Å}^3$ (0 GPa), 15.5730 $\text{Å}^3$ (10 GPa), 14.2759 $\text{Å}^3$ (20 GPa), 13.0530 $\text{Å}^3$ (30 GPa), 10.8206 $\text{Å}^3$, and 9.8069 $\text{Å}^3$ (120 GPa). (a) TDOS in a broad range of energies: from $-15$ eV to $+10$ eV. (b), (c) Zoomed-in TDOS at the Fermi level and the main peak in the valence band. (d)–(g) PDOS corresponding to the two extreme volumes 18.3981 $\text{Å}^3$ (0 GPa) and 9.8069 $\text{Å}^3$ (120 GPa).

The corresponding TDOS and PDOS for the MgZn compound are plotted in Fig. 8. TDOS [Fig. 8(a)] is shown as a function of the normalized volume per atom (VPA), corresponding to applied pressures between $P = 0$–120 GPa. As seen, there is a prominent peak in the valence band above $-10$ eV which responds to pressure by broadening and shifting at lower energies [Fig. 8(c)]. Analysis of the projections onto atomic $s$, $p$, $d$ orbitals [PDOS; Figs. 8(d)–8(g)] reveals that this pressure-sensitive peak is associated with the $d$ electrons. Furthermore, TDOS at the Fermi level shows clear suppression with decreasing VPA, in accordance with the band structure in Fig. 7. Inspection of the corresponding region in PDOS indicates that this reduction is mainly due to reduction in the corresponding the $s$ and $p$ weights of Mg. In general, PDOS shows broadening toward lower energies upon applying pressure.

## IV. CONCLUSIONS

We have employed a configurational cluster expansion method, Markov chain Monte Carlo search algorithm, and first-principles computations in the framework of DFT to determine the stable phases of Mg-Zn and Al-Zn binaries on both hexagonal-close-packed (hcp) and face-centered-cubic (fcc) lattice symmetries. In order to find the ground states, we have constructed several CE models, performed extensive searches in configuration space to systematically predict configurations close to ground state in the entire composition range, and carried out DFT calculations (optimizing cell and geometry) for predicted configurations. By tuning concentrations with the step of 1.5625% (64-atom system), we have found that $MgZn_3$, $Mg_{19}Zn_{45}$, MgZn, and $Mg_{34}Zn_{30}$, with the hcp symmetry, and $MgZn_3$ and MgZn, with the fcc symmetry, are the stable phases of the relaxed Mg-Zn binary, while Al-Zn has a positive formation energy throughout the entire composition range for both the hcp and fcc subject to zero/finite pressure. Our findings are in a good agreement with experimental observations where $MgZn_2$, $Mg_4Zn_7$, and MgZn compounds with the hexagonal symmetry are found to be the most stable phases of large enough precipitates [37,38,41–43].

For the hcp case, the increase of external pressure to $P \approx 10$ GPa results in $Mg_{19}Zn_{45}$ becoming unstable and $Mg_{34}Zn_{30}$ being less favorable. At pressure values on the order of 20 GPa, a new compound, $Mg_3Zn$, shows stability and becomes more stable at higher pressure values, while $Mg_{34}Zn_{30}$ turns unstable at pressure values larger than $\approx 30$ GPa. For the fcc convex hull, the $Mg_3Zn$ compound weakly touches the convex hull at $P \gtrsim 20$ GPa, whereas the other compounds remain stable throughout the entire pressure range 0–120 GPa. By visualizing the atomic structures of the stable compounds, we have found that the stable phases of the hcp alloys are

TABLE I. Free energy per atom (eV) and volume per atom ($\text{Å}^3$) for the Mg-Zn compositions in the hcp lattice.

| | | | | | Free energy: hcp | | | | | | |
|---|---|---|---|---|---|---|---|---|---|---|---|
| Pressure (GPa) | Zn | $Mg_{15}Zn_{49}$ | $MgZn_3$ | $Mg_{17}Zn_{47}$ | $Mg_{19}Zn_{45}$ | $Mg_{21}Zn_{43}$ | MgZn | $Mg_{34}Zn_{30}$ | $Mg_3Zn$ | $Mg_{61}Zn_3$ | Mg |
| 0 | −1.1913 | −1.3473 | −1.3586 | −1.3667 | −1.3838 | −1.3984 | −1.4853 | −1.4997 | −1.5507 | −1.6028 | −1.6155 |
| 10 | −1.1461 | −1.2931 | −1.3066 | −1.3111 | −1.3239 | −1.3369 | −1.4189 | −1.4285 | −1.4666 | −1.5002 | −1.5167 |
| 20 | −1.0632 | −1.1933 | −1.2051 | −1.2078 | −1.2151 | −1.2247 | −1.2941 | −1.2983 | −1.3137 | −1.3192 | −1.3297 |
| 30 | −0.9632 | −1.0738 | −1.0845 | −1.0850 | −1.0901 | −1.0964 | −1.1500 | −1.1439 | −1.1387 | −1.1154 | −1.1184 |
| 40 | −0.8539 | −0.9444 | −0.9541 | −0.9532 | −0.9550 | −0.9581 | −0.9962 | −0.9800 | −0.9553 | −0.9024 | −0.8991 |
| 70 | −0.4976 | −0.5333 | −0.5403 | −0.5346 | −0.5271 | −0.5214 | −0.5130 | −0.4935 | −0.3902 | −0.2562 | −0.2338 |
| 100 | −0.1254 | −0.1112 | −0.1143 | −0.1057 | −0.0906 | −0.0768 | −0.0273 | 0.0024 | 0.1702 | 0.3790 | 0.4164 |
| 120 | 0.1274 | 0.1695 | 0.1689 | 0.1793 | 0.1992 | 0.2179 | 0.2928 | 0.3296 | 0.5362 | 0.7901 | 0.8388 |
| | | | | | Volume: hcp | | | | | | |
| Pressure (GPa) | Zn | $Mg_{15}Zn_{49}$ | $MgZn_3$ | $Mg_{17}Zn_{47}$ | $Mg_{19}Zn_{45}$ | $Mg_{21}Zn_{43}$ | MgZn | $Mg_{34}Zn_{30}$ | $Mg_3Zn$ | $Mg_{61}Zn_3$ | Mg |
| 0 | 15.1025 | 16.4484 | 16.2846 | 16.6239 | 16.9157 | 17.1406 | 17.9532 | 18.6384 | 20.1345 | 22.4132 | 22.9254 |
| 10 | 13.4443 | 14.4160 | 14.3613 | 14.5454 | 14.7575 | 14.9387 | 15.5188 | 16.0125 | 17.0235 | 18.5934 | 18.9490 |
| 20 | 12.5345 | 13.2108 | 13.2517 | 13.3135 | 13.4257 | 13.5469 | 14.1554 | 14.5631 | 15.3522 | 16.6138 | 16.9017 |
| 30 | 11.8872 | 12.4360 | 12.4712 | 12.5180 | 12.6144 | 12.7148 | 13.2239 | 13.5661 | 14.2218 | 15.2960 | 15.5360 |
| 40 | 11.3845 | 11.8403 | 11.8717 | 11.9114 | 11.9934 | 12.0783 | 12.5161 | 12.8124 | 13.3791 | 14.3178 | 14.5297 |
| 70 | 10.3258 | 10.6168 | 10.6393 | 10.6651 | 10.7195 | 10.7778 | 11.0751 | 11.1598 | 11.6948 | 12.3911 | 12.5478 |
| 100 | 9.6188 | 9.8141 | 9.8288 | 9.8492 | 9.8897 | 9.9324 | 10.1504 | 10.2173 | 10.6290 | 11.1834 | 11.3116 |
| 120 | 9.2505 | 9.4047 | 9.4157 | 9.4335 | 9.4671 | 9.5027 | 9.6834 | 9.7407 | 10.0954 | 10.5841 | 10.6959 |

TABLE II. Free energy per atom (eV) and volume per atom ($\text{Å}^3$) for the Mg-Zn compositions in the fcc lattice.

| | | | Free energy: fcc | | | |
|---|---|---|---|---|---|---|
| Pressure (GPa) | Zn | $Mg_6Zn_{58}$ | $MgZn_3$ | MgZn | $Mg_3Zn$ | Mg |
| 0 | −1.1689 | −1.2336 | −1.3417 | −1.4805 | −1.5427 | −1.6085 |
| 10 | −1.1262 | −1.1859 | −1.2884 | −1.4144 | −1.4558 | −1.5000 |
| 20 | −1.0410 | −1.0925 | −1.1848 | −1.2817 | −1.2980 | −1.3095 |
| 30 | −0.9379 | −0.9810 | −1.0620 | −1.1358 | −1.1174 | −1.0966 |
| 40 | −0.8251 | −0.8610 | −0.9298 | −0.9840 | −0.9222 | −0.8738 |
| 50 | −0.7066 | −0.7352 | −0.7920 | −0.8234 | −0.7293 | −0.6500 |
| 60 | −0.5851 | −0.6067 | −0.6520 | −0.6732 | −0.5381 | −0.4266 |
| 70 | −0.4604 | −0.4754 | −0.5090 | −0.5021 | −0.3566 | −0.2021 |
| 80 | −0.3346 | −0.3434 | −0.3664 | −0.3333 | −0.1499 | 0.0187 |
| 90 | −0.2073 | −0.2107 | −0.2228 | −0.1718 | 0.0430 | 0.2375 |
| 100 | −0.0819 | −0.0778 | −0.0790 | −0.0073 | 0.2247 | 0.4537 |
| 120 | 0.1745 | 0.1880 | 0.2059 | 0.3153 | 0.5882 | 0.8770 |
| | | | Volume: fcc | | | |
| Pressure (GPa) | Zn | $Mg_6Zn_{58}$ | $MgZn_3$ | MgZn | $Mg_3Zn$ | Mg |
| 0 | 15.0892 | 15.6145 | 16.4053 | 18.0280 | 20.5353 | 23.0647 |
| 10 | 13.5633 | 13.9217 | 14.4742 | 15.5968 | 17.3198 | 19.0178 |
| 20 | 12.6312 | 12.9019 | 13.3414 | 14.1572 | 15.5902 | 16.9342 |
| 30 | 11.9649 | 12.1799 | 12.5467 | 13.2325 | 14.4226 | 15.5586 |
| 40 | 11.4460 | 11.6277 | 11.9385 | 12.5335 | 13.4950 | 14.5354 |
| 50 | 11.0239 | 11.1780 | 11.4474 | 11.9608 | 12.7777 | 13.7380 |
| 60 | 10.6699 | 10.8030 | 11.0391 | 11.5233 | 12.2199 | 13.0870 |
| 70 | 10.3625 | 10.4792 | 10.6865 | 11.1031 | 11.7821 | 12.5341 |
| 80 | 10.0940 | 10.1971 | 10.3821 | 10.7341 | 11.3736 | 12.0630 |
| 90 | 9.8541 | 9.9471 | 10.1114 | 10.4269 | 10.9933 | 11.6510 |
| 100 | 9.6427 | 9.7231 | 9.8691 | 10.1523 | 10.6538 | 11.2869 |
| 120 | 9.2688 | 9.3355 | 9.4537 | 9.6819 | 10.1333 | 10.6698 |

TABLE III.  Calculated bulk moduli of the Mg-Zn alloys.

| | | | | | $B_0$: hcp | | | | | |
| --- | --- | --- | --- | --- | --- | --- | --- | --- | --- | --- |
| Pressure (GPa) | Zn | $Mg_{15}Zn_{49}$ | $MgZn_3$ | $Mg_{17}Zn_{47}$ | $Mg_{19}Zn_{45}$ | $Mg_{21}Zn_{43}$ | MgZn | $Mg_{34}Zn_{30}$ | $Mg_3Zn$ | $Mg_{61}Zn_3$ | Mg |
| 0 | 66.6732 | 54.6725 | 60.6312 | 53.8911 | 51.0433 | 50.0149 | 50.8842 | 48.6929 | 42.8050 | 37.4733 | 36.5245 |

| | | | $B_0$: fcc | | | |
| --- | --- | --- | --- | --- | --- | --- |
| Pressure (GPa) | Zn | $Mg_6Zn_{58}$ | $MgZn_3$ | MgZn | $Mg_3Zn$ | Mg |
| 0 | 72.9948 | 66.3637 | 60.5714 | 50.9126 | 41.4331 | 35.8843 |

| | | | $B_0$: Experiment | | |
| --- | --- | --- | --- | --- | --- |
| Pressure (GPa) | Zn | $MgZn_3$ | MgZn | $Mg_3Zn$ | Mg |
| 0 | 70.0 | | | | 45.0 |

mixtures of Mg and Zn. Similarly, the fcc alloys with a high concentration of Zn are perfect mixtures of Mg and Zn, whereas in the MgZn and Mg-rich compounds the atomic configurations exhibit layered elemental ordering. Analysis of the bulk modulus, volume reduction, and free energy of these compounds under finite pressure shows that Zn-rich compositions are more stable and have greater hardness than those with a high concentration of Mg.

Our results suggest that by applying an appropriate external pressure into Al matrices containing Mg and Zn solutes, one may be able to control the type of the early-stage precipitates—being either Zn-rich or Mg-rich. As the Zn-rich solid clusters have larger bulk modulus than those of the Mg-rich ones, the external pressure at early stage clustering can control the overall hardness of the entire matrix and improve its resistance against external deformation.
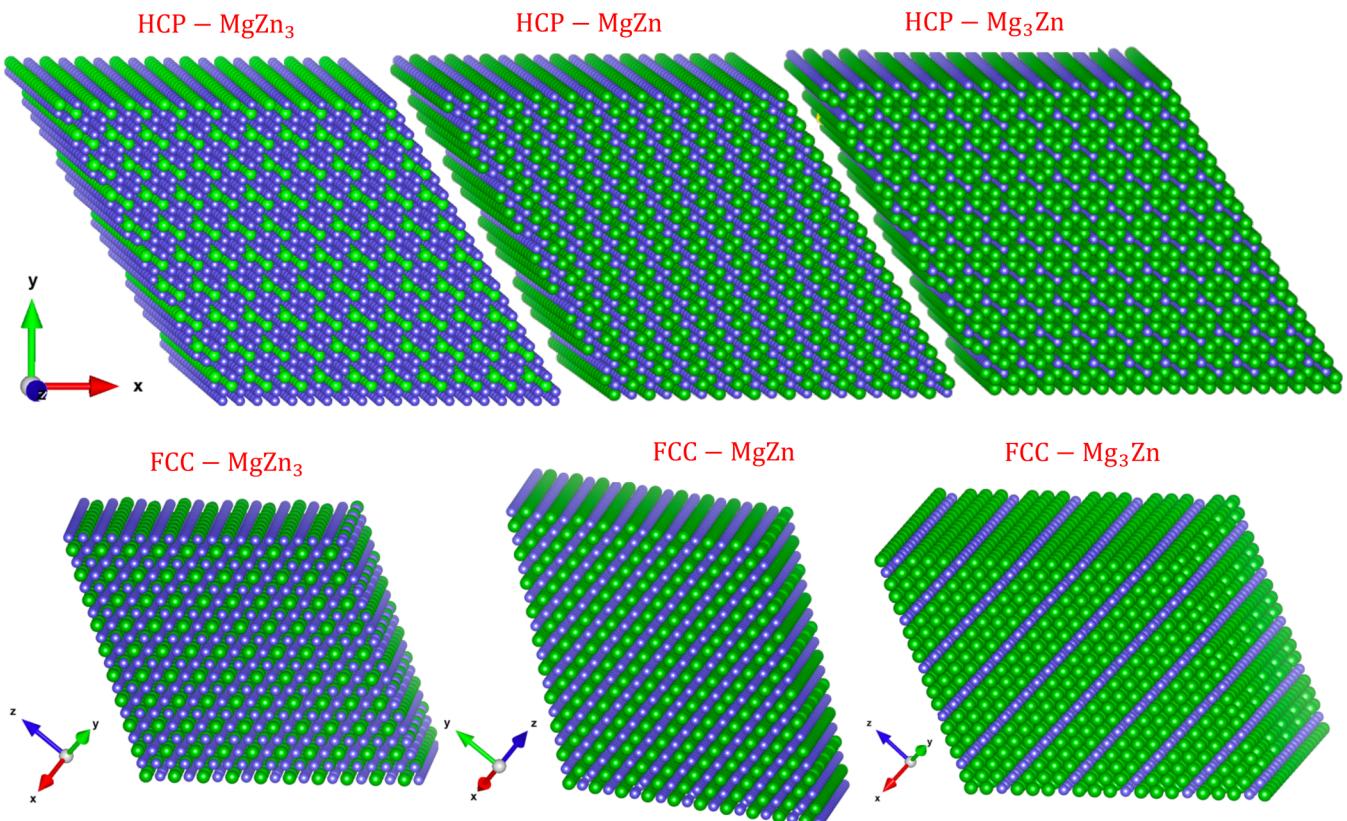


FIG. 9.  The high-symmetry hcp and fcc compositions of the Mg-Zn binary shown in the convex hull plots in the main text. The unit cells are replicated $5 \times 5 \times 5$ times.

## APPENDIX: FIRST-PRINCIPLES DATA AND EXTENDED UNIT CELLS

Here, we present the numerical results from DFT calculations for the Mg-Zn compounds discussed in the main text. Table I contains the normalized free energy of the Mg-Zn compounds with the hcp lattice symmetry. Table II presents the normalized free energy of the Mg-Zn compunds with the fcc lattice symmetry, and Table III summarizes the bulk moduli of several compositions on both the hcp and fcc lattices. We have also included the experimentally measured values for the bulk moduli.

To illustrate how the Mg and Zn elements are arranged in the high-symmetry compositions found in Figs. 1 and 2, we have expanded the unit cells of $MgZn_3$, $MgZn$, and $Mg_3Zn$ up to $5 \times 5 \times 5$ cells. We have rotated the cells for visualization purposes as the coordinate-axis arrows indicate in Fig. 9.

Also, Fig. 10 exhibits the DFT-calculated free energies of predicted unique structures for the Al-Zn alloys on both fcc and hcp lattices. The formation energy counterparts are presented in Fig. 3. In Fig. 10(a), the free energy of the Al-Zn alloys with the fcc lattice symmetry is plotted as a function of Mg concentration. The external pressure is set to zero. Figure 10(b) presents a similar study except now the lattice is changed to the hcp and the results of 40 GPa and 80 GPa
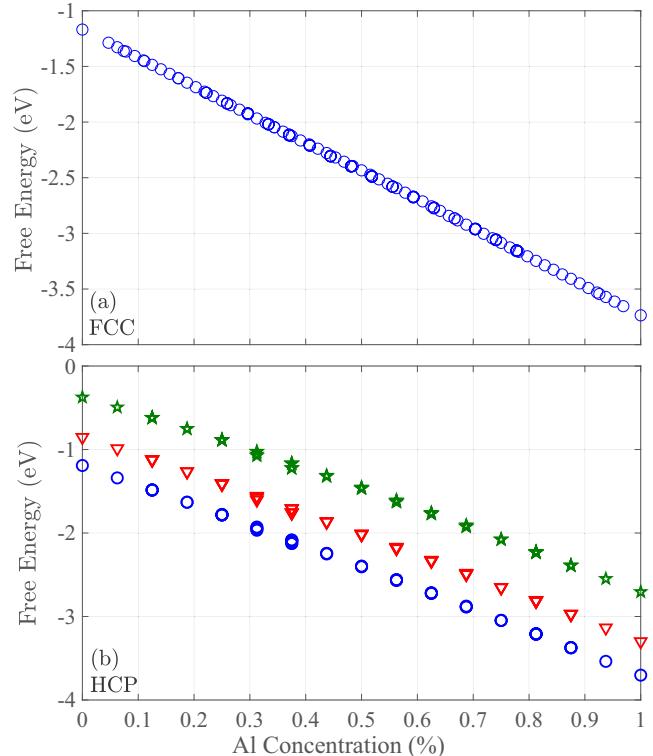


FIG. 10. Free energy of unique configurations of the Al-Zn binary as a function of Al concentration. (a) The fcc lattice with 163 unique configurations ($3 \times 3 \times 3$ and $4 \times 4 \times 4$ structures). The external pressure is set to zero. (b) The hcp lattice and 64 unique configurations under external pressure: $P = 0$ GPa (circles), 40 GPa (triangles), 80 GPa (asterisks).

pressure values in addition to 0 GPa are shown. The results show that the application of an isotropic static pressure to the Al-Zn alloys decreases the free energy.

[1] F. W. Gayle and M. Goodway, Precipitation hardening in the first aerospace aluminum alloy: The Wright flyer crankcase, Science **266**, 1015 (1994).

[2] T. M. Pollock, Weight loss with magnesium alloys, Science **328**, 986 (2010).

[3] J. F. Nie, Precipitation and hardening in magnesium alloys, Metall. Mater. Trans. A **43**, 3891 (2012).

[4] Z. Wu, M. F. Francis, and W. A. Curtin, Magnesium interatomic potential for simulating plasticity and fracture phenomena, Modell. Simul. Mater. Sci. Eng. **23**, 015004 (2015).

[5] Y.-M. Kim, N. J. Kim, and B.-J. Lee, Atomistic modeling of pure Mg and Mg-Al systems, CALPHAD: Comput. Coupling Phase Diagrams Thermochem. **33**, 650 (2009).

[6] P. Mao, B. Yu, Z. Liu, F. Wang, and Y. Ju, First-principles calculations of structural, elastic, and electronic properties of $AB_2$-type intermetallics in Mg-Zn-Ca-Cu alloy, J. Magnesium Alloys **1**, 256 (2013).

[7] D. E. Dickel, M. Baskes, I. Aslam and C. D. Barrett, New interatomic potential for Mg-Al-Zn alloys with specific application

to dilute Mg-based alloys, Modell. Simul. Mater. Sci. Eng. **26**, 045010 (2018).

[8] B. Zou, Z. Q. Chen, C. H. Liu, and J. H. Chen, Vacancy-Mg complexes and their evolution in early stages of aging of Al-Mg based alloys, Appl. Surf. Sci. **298**, 50 (2014).

[9] D. Kleiven, O. L. Ødegard, K. Laasonen, and J. Akola, Atomistic simulations of early stage clusters in Al-Mg alloys, Acta Mater. **166**, 484 (2019).

[10] B. Zheng, L. Zhaoa, X. B. Hua, S. J. Donga, and H. Li, First-principles studies of $Mg_{17}Al_{12}$, $Mg_2Al_3$, $Mg_2Sn$, $MgZn_2$, $Mg_2Ni$, $Al_3Ni$ phases, Phys. B (Amsterdam) **560**, 255 (2019).

[11] T. Tsurua, M. Yamaguchi, K. Ebihara, M. Itakura, Y. Shiihara, K. Matsuda, and H. Toda, First-principles study of hydrogen segregation at the $MgZn_2$ precipitate in Al-Mg-Zn alloys, Comput. Mater. Sci. **148**, 301 (2018).

[12] C. Ravi and C. Wolverton, First-principles study of crystal structure and stability of AlMgSi(Cu) precipitates, Acta Mater. **52**, 4213 (2004).

[13] A. V. Ruban and I. A. Abrikosov, Configurational thermodynamics of alloys from first principles: Effective cluster interactions, Rep. Prog. Phys. **71**, 046501 (2008).

[14] A. Yu. Stroev, O. I. Gorbatov, Yu. N. Gornostyrev, and P. A. Korzhavyi, Solid solution decomposition and Guinier-Preston zone formation in AlCu alloys: A kinetic theory with anisotropic interactions, Phys. Rev. Materials **2**, 033603 (2018).

[15] H.-S. Jang, K.-M. Kim, and B.-J. Lee, Modified embedded-atom method interatomic potentials for pure Zn and Mg-Zn binary system, CALPHAD: Comput. Coupling Phase Diagrams Thermochem. **60**, 200 (2018).

[16] M. I. Baskes, Commentary on 'modified embedded atom method potentials for hcp metals', Modell. Simul. Mater. Sci. Eng. **25**, 071002 (2017).

[17] J. M. Sanchez, Cluster expansion and the configurational theory of alloys, Phys. Rev. B **81**, 224202 (2010).

[18] S. Wang, Y. Zhao, H. Guo, F. Lan, and H. Hou, Mechanical and thermal conductivity properties of enhanced phases in Mg-Zn-Zr system from first principles, Materials **11**, 2010 (2018).

[19] Y. Z. Ji, A. Issa, T. W. Heo, J. E. Saal, C. Wolverton, and L. Q. Chen, Predicting $\beta'$ precipitate morphology and evolution in Mg-*RE* alloys using a combination of first-principles calculations and phase-field modeling, Acta Mater. **76**, 259 (2014).

[20] T. E. M. Staab, B. Klobes, I. Kohlbach, B. Korff, M. Haaks, E. Dudzik, and K. Maier, Atomic structure of pre-Guinier-Preston and Guinier-Preston-Bagaryatsky zones in Al alloys, J. Phys.: Conf. Ser. **265**, 012018 (2011).

[21] S. R. Nayak, C. J. Hung, R. J. Hebert, and S. P. Alpay, Atomistic origins of Guinier-Preston zone formation and morphology in Al-Cu and Al-Ag alloys from first principles, Scr. Mater. **162**, 235 (2019).

[22] G. Yi, W. Zeng, J. D. Poplawsky, D. A. Cullen, Z. Wang, and M. L. Free, Characterizing and modeling the precipitation of Mg-rich phases in Al 5xxx alloys aged at low temperatures, J. Mater. Sci. Technol. **33**, 991 (2017).

[23] M. Liu, H. Fu, L. Tian, W. Xiao, Q. Peng, and C. Ma, Nucleation and growth mechanisms of nano-scaled Si precipitates in Al-7Si supersaturated solid solution, Mater. Des. **121**, 373 (2017).

[24] C. Wang, T.-L. Huang, H.-Y. Wang, X.-N. Xue, and Q.-C. Jiang, Effects of distributions of Al, Zn, and Al+Zn atoms on the strengthening potency of Mg alloys: A first-principles calculation, Comput. Mater. Sci. **104**, 23 (2015).

[25] G. Esteban-Manzanares, A. Ma, I. Papadimitriou, E. Martínez, and J. Llorca, Basal dislocation/precipitate interactions in Mg-Al alloys: An atomistic investigation, Modell. Simul. Mater. Sci. Eng. **27**, 075003 (2019).

[26] T. Saito, E. A. Mørtsell, S. Wenner, C. D. Marioara, S. J. Andersen, J. Friis, K. Matsuda, and R. Holmestad, Atomic structures of precipitates in Al-Mg-Si alloys with small additions of other elements, Adv. Eng. Mater. **20**, 1800125 (2018).

[27] S. J. Andersen, C. D. Marioara, J. Friis, S. Wenner, and R. Holmestad, Precipitates in aluminium alloys, Adv. Phys. X **3**, 1479984 (2018).

[28] T. Saito, S. Wenner, E. Osmundsen, C. D. Marioara, S. J. Andersen, J. Røyset, W. Lefebvre, and R. Holmestad, The effect of Zn on precipitation in Al-Mg-Si alloys, Philos. Mag. **94**, 2410 (2014).

[29] W. Chrominski, S. Wenner, C. D. Marioara, R. Holmestad, and M. Lewandowska, Strengthening mechanisms in ultrafine-grained Al-Mg-Si alloy processed by hydrostatic extrusion: Influence of ageing temperature, Mater. Sci. Eng. **669**, 447 (2016).

[30] E. Christiansen, C. D. Marioara, K. Marthinsen, O. S. Hopperstad, and R. Holmestad, Lattice rotations in precipitate free zones in an Al-Mg-Si alloy, Mater. Charac. **144**, 522 (2018).

[31] Y. Xin, X. Zhou, H. Chen, J.-F. Nie, H. Zhang, Y. Zhang, and Q. Liu, Annealing hardening in detwinning deformation of Mg-3Al-1Zn alloy, Mater. Sci. Eng. A **594**, 287 (2014).

[32] W. Lefebvre, V. Kopp, and C. Pareige, Nano-Precipitates Made of Atomic Pillars Revealed by Single Atom Detection in a Mg-Nd Alloy, Appl. Phys. Lett. **100**, 141906 (2012).

[33] X. Gao and J. F. Nie, Enhanced precipitation-hardening in Mg-Gd alloys containing Ag and Zn, Scr. Mater. **58**, 619 (2008).

[34] J. F. Nie, N. C. Wilson, Y. M. Zhu, and Z. Xu, Solute clusters and GP zones in binary Mg-Re alloys, Acta Mater. **106**, 260 (2016).

[35] H. D. Zhao, G. W. Qin, Y. P. Ren, W. L. Pei, D. Chen, and Y. Guo, The maximum solubility of Y in $\alpha$-Mg and composition ranges of $Mg_{24}Y_{5-x}$ and $Mg_2Y_{1-x}$ intermetallic phases in Mg-Y binary system, J. Alloys Compd **509**, 627 (2011).

[36] W. Sun, Y. Zhu, R. Marceau, L. Wang, Q. Zhang, X. Gao, and C. Hutchinson, Precipitation strengthening of aluminum alloys by room-temperature cyclic plasticity, Science **363**, 972 (2019).

[37] A. Bendo, T. Maeda, K. Matsuda, A. Lervik, R. Holmestad, C. D. Marioara, K. Nishimura, N. Nunomura, H. Toda, M. Yamaguchi, K.-i. Ikeda, and T. Homma, Characterisation of structural similarities of precipitates in Mg-Zn and Al-Zn-Mg alloys systems, Philos. Mag. **99**, 2619 (2019).

[38] A. Lervik, C. D. Marioara, M. Kadanik, J. C. Walmsley, B. Milkereit, and R. Holmestad, Precipitation in an extruded AA7003 aluminium alloy: Observations of 6xxx-type hardening phases, Mater. Des. **186**, 108204 (2020).

[39] H. Okamoto, Comment on Mg-Zn (magnesium-zinc), J. Phase Equilib. **15**, 129 (1994).

[40] J. Peng, L.Zhong, Y. Wang, Y. Lu, and F. Pan, Effect of extrusion temperature on the microstructure and thermal conductivity of $Mg_{2.0}Zn_{1.0}Mn_{0.2}Ce$ alloys, Mater. Des. **87**, 914 (2015).

[41] A. Singh and J. Rosalie, Lattice correspondence and growth structures of monoclinic $Mg_4Zn_7$ phase growing on an icosahedral quasicrystal, Crystals **8**, 194 (2018).

[42] T.-F. Chung, Y.-L. Yang, B.-M. Huang, Z. Shi, J. Lin, T. Ohmura, and J.-R. Yang, Transmission electron microscopy investigation of separated nucleation and in-situ nucleation in AA7050 aluminium alloy, Acta Mater. **149**, 377 (2018).

[43] W. Liu, H. Zhao, D. Li, Z. Zhang, G. Huang, and Q. Liu, Hot deformation behavior of AA7085 aluminum alloy during isothermal compression at elevated temperature, Mater. Sci. Eng. A **596**, 176 (2014).

[44] B. Sun, Y. Dong, J. Tan, H. Zhang, and Y. Sun, Direct observation of $\beta''$ precipitate with a three-dimensional periodic structure in binary Mg-La alloy, Mater. Des. **181**, 107939 (2019).

[45] S. DeWitt, E. L. S. Solomon, A. R. Natarajan, V. Araullo-Peters, S. Rudraraju, L. K. Aagesen, B. Puchala, E. A. Marquis,

A. van der Ven, K. Thornton, and J. E. Allison, Misfit-driven $\beta'''$ precipitate composition and morphology in Mg-Nd alloys, Acta Mater. **136**, 378 (2017).

[46] E. L. S. Solomon, A. R. Natarajan, A. M. Roy, V. Sundararaghavan, A. Van der Ven, and E. A. Marquis, Stability and strain-driven evolution of $\beta'$ precipitate in Mg-Y alloys, Acta Mater. **166**, 148 (2019).

[47] P. Ma, C. M. Zou, H. W. Wang, S. Scudino, K. K. Song, M. S. Khoshkhoo, Z. J. Wei, U. Kuhn, and J. Eckert, Structure of GP zones in AlSi matrix composites solidified under high pressure, Mater. Lett. **109**, 1 (2013).

[48] J.-Y. Wang, N. Li, R. Alizadeh, M. A. Monclus, Y. W. Cui, J. M. Molina-Aldareguia, and J. LLorca, Effect of solute content and temperature on the deformation mechanisms and critical resolved shear stress in Mg-Al and Mg-Zn alloys, Acta Mater. **170**, 155 (2019).

[49] J. J. Mortensen, L. B. Hansen, and K. W. Jacobsen, Real-space grid implementation of the projector augmented wave method, Phys. Rev. B **71**, 035109 (2005).

[50] J. Enkovaara, C. Rostgaard, J. J. Mortensen, J. Chen, M. Dułak, L. Ferrighi, J. Gavnholt, C. Glinsvad, V. Haikola, H. A. Hansen *et al.*, Electronic structure calculations with GPAW: A real-space implementation of the projector augmented-wave method, J. Phys.: Condens. Matter **22**, 253202 (2010).

[51] A. H. Larsen, J. J. Mortensen, J. Blomqvist, I. E. Castelli, R. Christensen, M. Dułak, J. Friis, M. N. Groves, B. Hammer, C. Hargus *et al.*, The atomic simulation environment: A Python library for working with atoms, J. Phys.: Condens. Matter **29**, 273002 (2017).

[52] D. B. Laks, L. G. Ferreira, S. Froyen, and A. Zunger, Efficient cluster expansion for substitutional systems, Phys. Rev. B **46**, 12587 (1992).

[53] M. Asta, C. Wolverton, D. De Fontaine, and H. Dreysse, Effective cluster interactions from cluster-variation formalism, Phys. Rev. B **44**, 4907 (1991).

[54] J. H. Chang, D. Kleiven, M. Melander, J. Akola, J. M. G. Lastra, and T. Vegge, CLEASE: A versatile and user-friendly implementation of cluster expansion method, J. Phys.: Condens. Matter **31**, 325901 (2019).

[55] J. Zhang, X. Liu, S. Bi, J. Yin, G. Zhang, and M. Eisenbach, Robust data-driven approach for predicting the configurational energy of high entropy alloys, Materials & Design **185**, 108247 (2020).

[56] O. I. Gorbatov, A. Yu Stroev, Yu. N. Gornostyrev, and P. A. Korzhavyi, Effective cluster interactions and precipitate morphology in binary Al-based alloys, Acta Mater. **179**, 70 (2019).

[57] M. Yu. Lavrentiev, R. Drautz, D. Nguyen-Manh, T. P. C. Klaver, and S. L. Dudarev, Monte Carlo study of thermodynamic properties and clustering in the bcc Fe-Cr system, Phys. Rev. B **75**, 014208 (2007).

[58] J. S. Wrobel, D. Nguyen-Manh, M. Yu. Lavrentiev, M. Muzyk, and S. L. Dudarev, Phase stability of ternary fcc and bcc Fe-Cr-Ni alloys, Phys. Rev. B **91**, 024108 (2015).

[59] N. Metropolis and S. Ulam, The Monte Carlo Method, J. Am. Stat. **44**, 335 (1949).

[60] S. L. Chen and Y. A. Chang, A thermodynamic analysis of the Al-Zn system and phase diagram calculation, CALPHAD: Comput. Coupling Phase Diagrams Thermochem. **17**, 113 (1993).